

Article

Enhanced Photocatalytic and Antibacterial Performance of ZnO Nanoparticles Prepared by an Efficient Thermolysis Method

Md. Abu Hanif ^{1,*}, Insup Lee ¹, Jeasmin Akter ², Md. Akherul Islam ¹, Ali A. S. M. Zahid ³, Kamal Prasad Sapkota ¹ and Jae Ryang Hahn ^{1,4,*}

¹ Department of Chemistry and Bioactive Material Sciences, Research Institute of Physics and Chemistry, Chonbuk National University, Jeonju 54896, Korea

² Department of Chemistry, Faculty of Civil Engineering, Khulna University of Engineering & Technology, Khulna 9203, Bangladesh

³ Department of Chemistry, Faculty of Science, University of Rajshahi, Rajshahi-6205, Bangladesh

⁴ Textile Engineering, Chemistry and Science, North Carolina State University, 2401 Research Dr. Raleigh, NC 27695-8301, USA

* Correspondence: hanif4572@gmail.com (M.A.H.); jrhanh@jbnu.ac.kr (J.R.H.); Tel.: +82-63-270-3406 (J.R.H.)

Received: 3 June 2019; Accepted: 15 July 2019; Published: 18 July 2019



Abstract: ZnO nanoparticles (ZnO-NPs) were synthesized by a straightforward modified thermal method using only one chemical: zinc acetate dihydrate. The process is environmentally safer than other methods because it does not involve other chemicals or a catalyst, acid, or base source. X-ray diffraction analysis indicated that the ZnO-NPs crystallize in the hexagonal wurtzite structure. The UV–vis absorption spectra revealed a marked redshift, which is critical for enhanced photocatalytic activity. We used methylene blue for photocatalytic activity tests and found an excellent degradation percentage (99.7%) within a short time (80 min). The antibacterial activity of the synthesized ZnO-NPs was tested against *Escherichia coli* at different concentrations of ZnO-NPs. The analysis revealed that the minimum inhibitory concentration (MIC) of the ZnO-NPs against *E. coli* was 30–50 µg/mL. Our ZnO-NPs were found to be more effective than previously reported ZnO-NPs synthesized via other methods.

Keywords: ZnO nanoparticles; thermal method; photocatalytic activity; antibacterial activity

1. Introduction

ZnO is a nontoxic semiconductor material with a wide bandgap (3.37 eV) and a high exciton binding energy (60 meV) [1]. Thus, ZnO nanoparticles (ZnO-NPs) have been used as, for example, photocatalysts for organic pollutant degradation [2], antibiotics [3,4], electrode materials for solar cells [5], and photoluminescence emitters [6]. Due to the various applications of ZnO-NPs, researchers have attempted to synthesize them using methods such as chemical vapor deposition [7], microemulsion-mediated synthesis [8], and electrodeposition [9]. However, the main disadvantage of these methods is that they involve harmful chemicals, expensive catalysts, and/or complicated techniques.

Among the many characteristics of ZnO, two of the most interesting are photocatalytic activity and antibacterial activity. Both of these properties are related to environmental contamination and are critical for maintaining clean water and preserving human life. The major sources of water contamination are organic dyes and water wastes, which mainly originate from wastewater treatment plants. Organic dyes remain unaffected in the aquatic environment because of their excellent stability against heat, light, microbial attack, and chemical degradation [10]. Thus, metal oxide photocatalysts,

such as ZnO and TiO₂, are attractive materials for the degradation of such organic pollutants in the presence of UV light and/or solar radiation [11]. The photocatalytic activity of ZnO is apparently better than that of TiO₂ because ZnO exhibits greater electron mobility [12]. This higher electron mobility may enhance the migration rate of photogenerated electrons in ZnO and obstruct the recombination of photogenerated electrons and holes, thereby increasing the lifetime of the photogenerated charge carriers [12]. To attain efficient photocatalytic activity, a large amount of pristine ZnO is required [13]. Hence, a facile technique for enhancing the performance of ZnO such that it can be used in smaller quantities is urgently needed.

Furthermore, inorganic metal oxides (e.g., MgO, CaO, ZnO, and TiO₂) can function as antimicrobial agents [14]. Recently, ZnO has been reported to exhibit notable activity against bacteria, microfungi, and viruses [3,4]. Only a small concentration of ZnO-NPs is needed to strongly inhibit the growth of pathogenic microbes. The antibacterial activity of ZnO-NPs has been attributed primarily to electrostatic contact between the bacterial cell surface and nanoparticles [14]. In addition, the low toxicity and strong UV-radiation absorption ability of ZnO-NPs further enhance their attractiveness as an antibacterial agent [14]. However, the mechanism by which ZnO-NPs interact with biomolecules and microorganisms remains unclear. Thus, the development of an effective method to apply ZnO-NPs as an antibiotic is needed.

In this study, we present a straightforward method to prepare ZnO-NPs that exhibit enhanced photocatalytic and antibacterial performance compared with ZnO-NPs prepared by other methods. Compared with other synthesis methods, ours is simple and eco-friendly. The thermolysis of zinc acetate dihydrate (Zn(CH₃COO)₂·2H₂O; ZAD) under high temperatures and pressures led to ZnO-NPs with high crystallinity and a nearly spherical morphology. Under UV light, the prepared ZnO-NPs show excellent photocatalytic activity toward the degradation of methylene blue (MB). Furthermore, the antibacterial activity of the synthesized ZnO-NPs was tested against *Escherichia coli* (Gram-negative) pathogenic microbial strain.

2. Results and Discussion

2.1. Structure, Morphology, and Composition of the Prepared ZnO-NPs

The prepared ZnO-NPs were indexed as hexagonal-wurtzite-structured ZnO. Figure 1 shows the X-ray diffraction (XRD) patterns of the (a) synthesized ZnO-NPs, (b) pure ZnO, and (c) the ZAD. The peak position, intensity, width, and full-width at half-maximum (FWHM) data were analyzed. The diffraction peaks were observed at 31.74°, 34.38°, 36.22°, 47.48°, 56.54°, 62.79°, 66.33°, 67.90°, 69.04°, 72.51°, 76.90°, 81.37°, and 89.56°—these peaks are attributed to the (100), (002), (101), (102), (110), (113), (200), (112), (201), (004), (202), (104), and (203) lattice plates of ZnO, respectively, as shown in Figure 1a. All of the peaks were clearly matched with those of pure ZnO (as shown in Figure 1b). Thus, the prepared ZnO-NPs were indexed to the hexagonal wurtzite structure of ZnO (JCPDS, No. 36-1451, lattice constants $a = 3.249 \text{ \AA}$ and $c = 5.206 \text{ \AA}$) [9,15]. No other characteristic peaks of the prepared ZnO-NPs were observed, indicating that our prepared ZnO-NPs consisted of a single pure phase, free of impurities such as Zn(OH)₂. Figure 1c shows the XRD pattern of the ZAD. After the sample was heated, its XRD pattern changed to match that of ZnO. Thus, the successful preparation of ZnO-NPs from ZAD was confirmed.

The crystal size (D) of the prepared ZnO-NPs was calculated using the Debye–Scherrer method [16]. A Gaussian–Lorentzian fitting program was used to fit the curves. The average size of the prepared ZnO-NPs was calculated to be 21.31 nm. With decreasing FWHM and increasing intensity of the ZnO-NP XRD peaks (increasing peak sharpness), the crystal size and crystallinity of the sample both increased.

The morphology of the prepared ZnO-NPs and pure ZnO were analyzed by field-emission scanning electron microscopy (FE-SEM). Figure 2a,b shows a low-magnification (10,000×) and a high-magnification (50,000×) image of the prepared ZnO-NPs, respectively. The prepared ZnO-NPs'

morphology, particle size, and aspect ratio were measured by FE-SEM analysis. The prepared ZnO-NPs were versatile, aggregated into nearly spherical shapes, and smooth. Figure S1a,b shows low- and high-magnification images of the pure ZnO (ACS reagent). Compared with the prepared ZnO-NPs, the pure ZnO is larger (approximately 149 nm) with a hexagonal rod-like shape (more than 30 images were compared for each sample). The nearly aggregated spherical shape of the ZnO-NPs enhanced their photocatalytic activity (discussed in detail in Section 2.2).

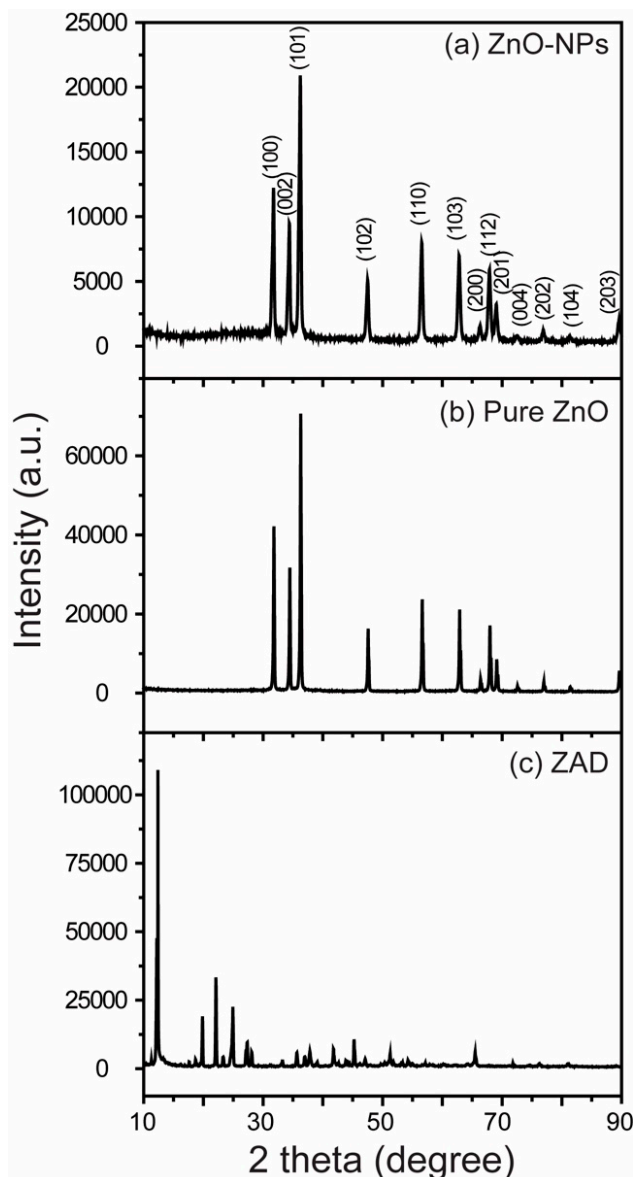


Figure 1. X-ray diffraction (XRD) patterns of the (a) synthesized ZnO-NPs, (b) pure ZnO, and (c) zinc acetate dihydrate (ZAD).

The energy dispersive X-ray spectroscopy (EDS) spectrum reveals the elemental composition of the prepared ZnO-NPs. Figure 2c shows the region selected for EDS analysis, and the corresponding EDS spectrum is shown in Figure 2d. Peaks of Zn, O, and Si were observed at approximately 1.01, 0.60, and 1.75 keV, respectively. The inset table in Figure 3d confirms the presence of Zn, O, and Si in wt% and at%. The Si peak is from the Si plate used for the FE-SEM sample.

The prepared ZnO-NPs were further observed by transmission electron microscopy (TEM) to characterize their atomic structure, size, fringe spacing, and morphology. Figure 3a shows a TEM image of several ZnO-NPs, and the inset shows their particle size distribution based on measurements from

the TEM image (calculated from 30 images). The TEM image shows that the prepared ZnO-NPs are nearly spherical, consistent with the FE-SEM results. The size distribution indicates that the ZnO-NPs vary from 58 to 167 nm and that the average size is 119 nm (averaged for ten particles observed in Figure 3a). The TEM images of the pure ZnO are presented in Figure S2a,b. The particles of pure ZnO were rod-shaped and larger than the ZnO-NPs, consistent with the FE-SEM results. The selected-area electron diffraction (SAED) pattern in Figure 3b shows the spot diffraction pattern with a very clear phase, confirming the high-quality single-crystalline structure of the prepared ZnO-NPs. This result is consistent with the XRD analysis results.

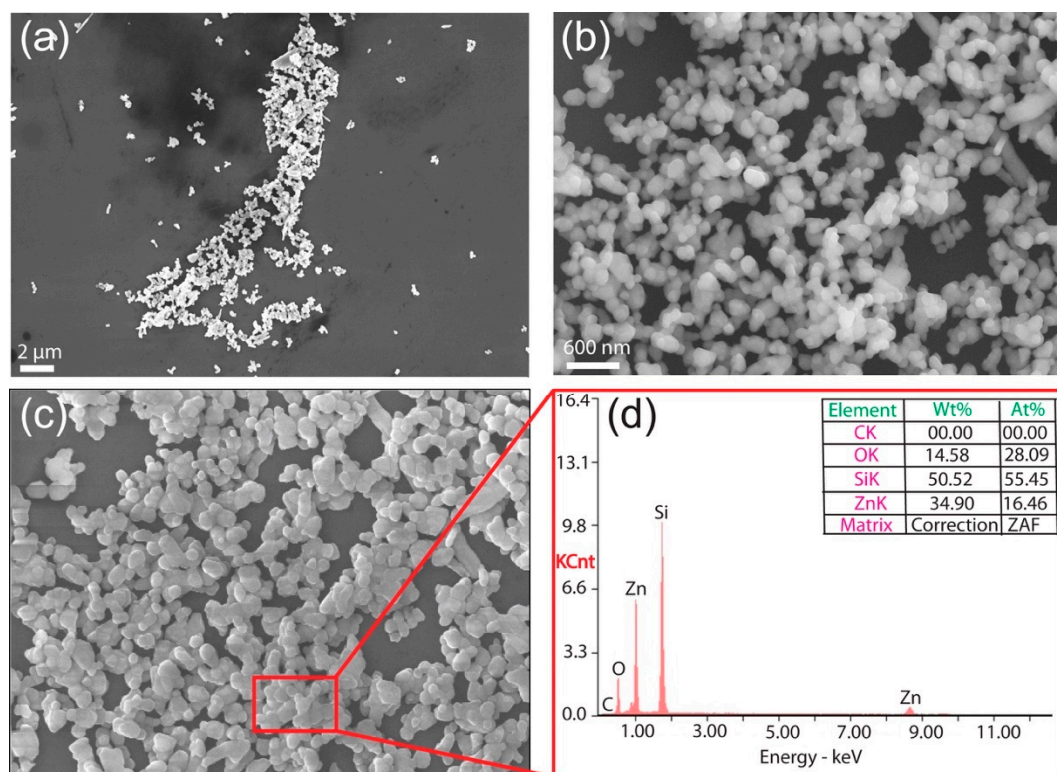


Figure 2. (a) and (b) field-emission scanning electron microscopy (FE-SEM) images of the prepared ZnO-NPs at different magnifications; (c) FE-SEM image showing the region selected for EDS analysis and (d) the corresponding EDS spectrum of the ZnO-NPs.

The high-resolution transmission electron microscopy (HR-TEM) images (Figure 3c) show the lattice pattern of a single-crystalline phase. Figure 3d shows an inverse fast Fourier transform (IFFT) spectrum corresponding to the rectangular region drawn in Figure 3c, which gives the d -spacing (see Figure 3e for a profile). The lattice spacing between two (0001) crystalline planes was 0.52 nm, consistent with that of the wurtzite hexagonal ZnO structure [17,18].

UV–vis absorption spectroscopy can be used to characterize the optical properties of nanoparticles. Figure 4 presents the UV–vis absorption spectrum of the synthesized ZnO-NPs at room temperature. The sharp UV–vis absorption peak at 383 nm (3.23 eV) is redshifted from that of pure ZnO (362 nm) [19], this redshift is apparently related to enhanced light absorption of nanoparticles. The absorption spectrum of the compound also provides information about the UV-light absorption and enhanced photocatalytic activity of the ZnO-NPs. This peak is assigned to the intrinsic bandgap absorption of ZnO. Electron transitions are known to occur from the $2p$ orbital of oxygen to the $3d$ orbital of Zn [valence band (VB) to conduction band (CB), $O_{2p} \rightarrow Zn_{3d}$] [20]. The sharp peak indicates that the synthesized ZnO-NPs are nanosized and that their size distribution is narrow. Both of these traits are beneficial with respect to photocatalytic and antibacterial activity. From Planck's energy equation, the bandgap of the synthesized nanoparticles was calculated to be 3.23 eV, which is slightly smaller

than the actual bandgap, i.e., 3.37 eV. The bandgap of 3.23 eV was calculated from the Tauc plot (Figure 4). No other significant peak was observed in the UV-vis spectrum, further indicating that the synthesized compound was composed only of ZnO.

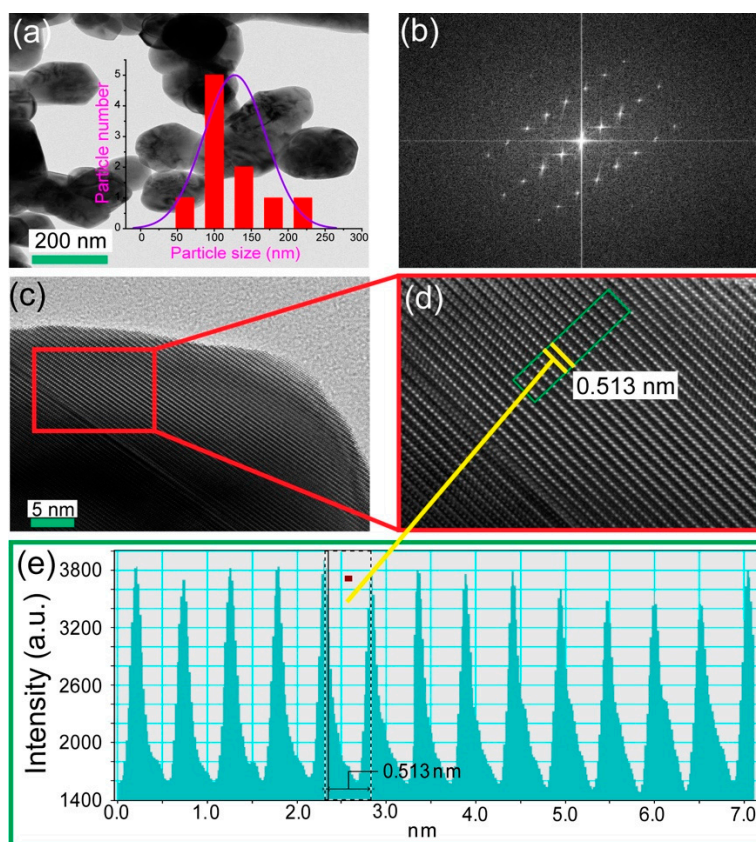


Figure 3. (a) Typical transmission electron microscopy (TEM) image of synthesized ZnO-NPs; the inset shows the corresponding particle size distribution of the ZnO-NPs. (b) The selected-area electron diffraction (SAED) pattern, (c) high-resolution TEM image, (d) inverse fast Fourier transform (IFFT) spectrum, and (e) profile of the IFFT image in (d).

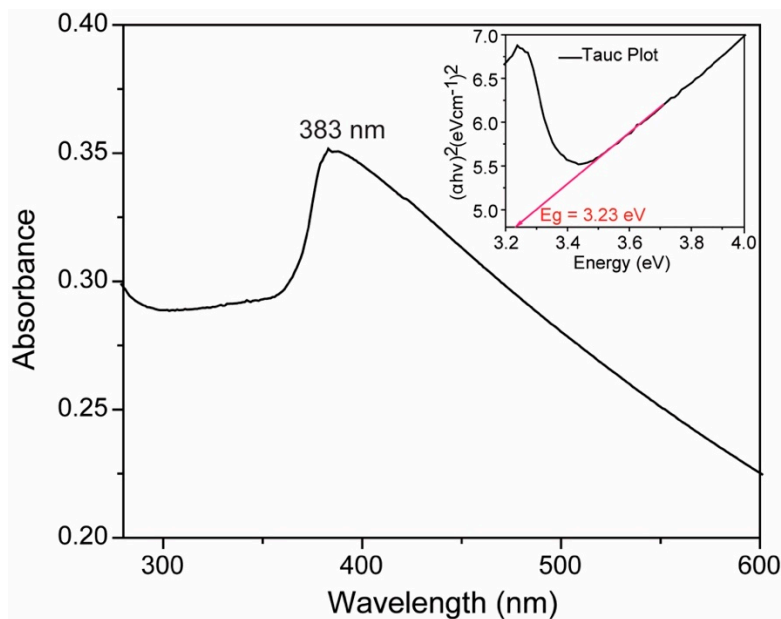


Figure 4. UV-vis absorption spectrum of synthesized ZnO-NPs, the inset shows the corresponding Tauc plot.

Thermogravimetry/differential thermal analysis (TG/DTA) was performed to confirm the formation and determine the thermal stability of a stable ZnO phase. Figure 5 displays the TG/DTA curve of ZAD, as recorded at a heating rate of 10 °C/min between 50 and 800 °C with the sample under a nitrogen (N₂) atmosphere. The thermal decomposition of the ZAD occurs in several steps, and 6.43% residue remains after thermal analysis to 800 °C. The first weight loss of 16.17% from room temperature to 110 °C is due to thermal dehydration of ZAD. By this thermal hydration, two water molecules per formula unit are lost, which is consistent with the theoretical value (16.41%) [21]. Upon further heating to 320 °C, the sample exhibited a second weight loss of 13.18% and a final weight loss of 64.23%. These results are attributed to the decomposition of zinc organic components. No further weight loss was observed upon further heating to 800 °C. In the DTA analysis, the two endothermic peaks at 95 and 248 °C are likely due to water loss and zinc organic decomposition, respectively.

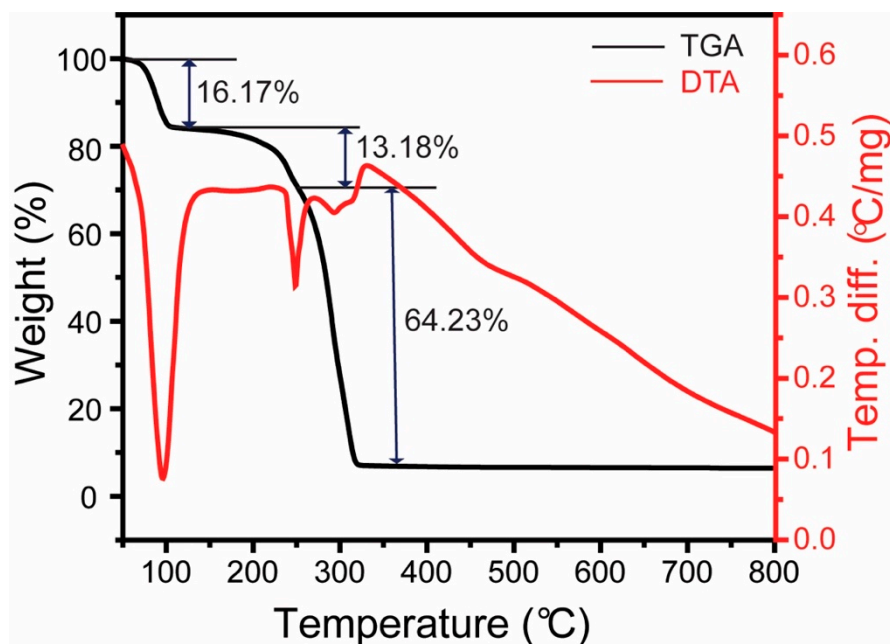


Figure 5. Thermogravimetry/differential thermal analysis (TG/DTA) of the ZAD.

2.2. Photocatalytic Performance of the Prepared ZnO-NPs

The UV–vis absorption spectra for the decomposition of MB under UV irradiation were recorded in the presence or absence of ZnO-NPs at 0, 5, 10, 20, 30, 40, 70, and 80 min, respectively (Figure 6). We observed that the absorption peak intensity of the MB dye at 664 nm gradually decreased with increasing irradiation time. That is, the MB particles were degraded by the ZnO catalyst, and the MB was almost completely degraded in 80 min in the presence of the ZnO-NPs.

The efficiency of the photodegradation (percentage) of MB in the presence or absence of ZnO-NPs was calculated via Equation (1) [22]:

$$\eta = \frac{C_0 - C_t}{C_0} \times 100 \quad (1)$$

where η is the degradation rate, C_0 is the absorbance at 0 min, and C_t is the absorbance at decomposition time t . Figure 6d presents the decomposition rates of MB in the presence and absence of ZnO-NPs. The degradation rate at 5, 10, 20, 30, 40, 70, and 80 min was 10.6%, 34.4%, 49.8%, 68.3%, 80.8%, 98.4%, and 99.7%, respectively, for the ZnO-NPs. These results indicate that ~50% of the MB dye was degraded within 20 min and that 99.7% of the MB dye was degraded within 80 min when the ZnO-NPs were used. By contrast, 8.6% and 19.1% of the MB dye was degraded within 20 min and 80 min, respectively, in the absence of ZnO-NPs.

We compared the photodegradation performance of the ZnO-NPs with the results reported for ZnO-NPs prepared by other methods, as shown in Table 1. Some of the previously reported ZnO-NP catalysts were prepared by a biological method, and their photocatalytic activity was tested using different dyes such as methyl red and MB [2,23,24]. These photocatalysts required longer degradation times (180 min, 90 min) to degrade the dyes and their degradation rates were moderately low (92.5%, 83.45%, and 97%). Even the chemically synthesized ZnO and Sr-doped ZnO required a long degradation time (120 min) and exhibited a relatively lower degradation rate (37% and 78.5%, respectively) when tested with MB [10,25]. Therefore, from the results in Table 1, we conclude that all of the previously reported ZnO photocatalysts required a longer reaction time to degrade the dye and that their degradation rates were comparatively low. By contrast, the photocatalyst synthesized by our method (modified thermal method) demonstrated a high degradation efficiency (99.7%) within a short time (80 min). Hence, our synthesized ZnO-NPs showed excellent photocatalytic activity toward

dye degradation compared with both the previously reported ZnO nanoparticles and the pure ZnO investigated in the present work.

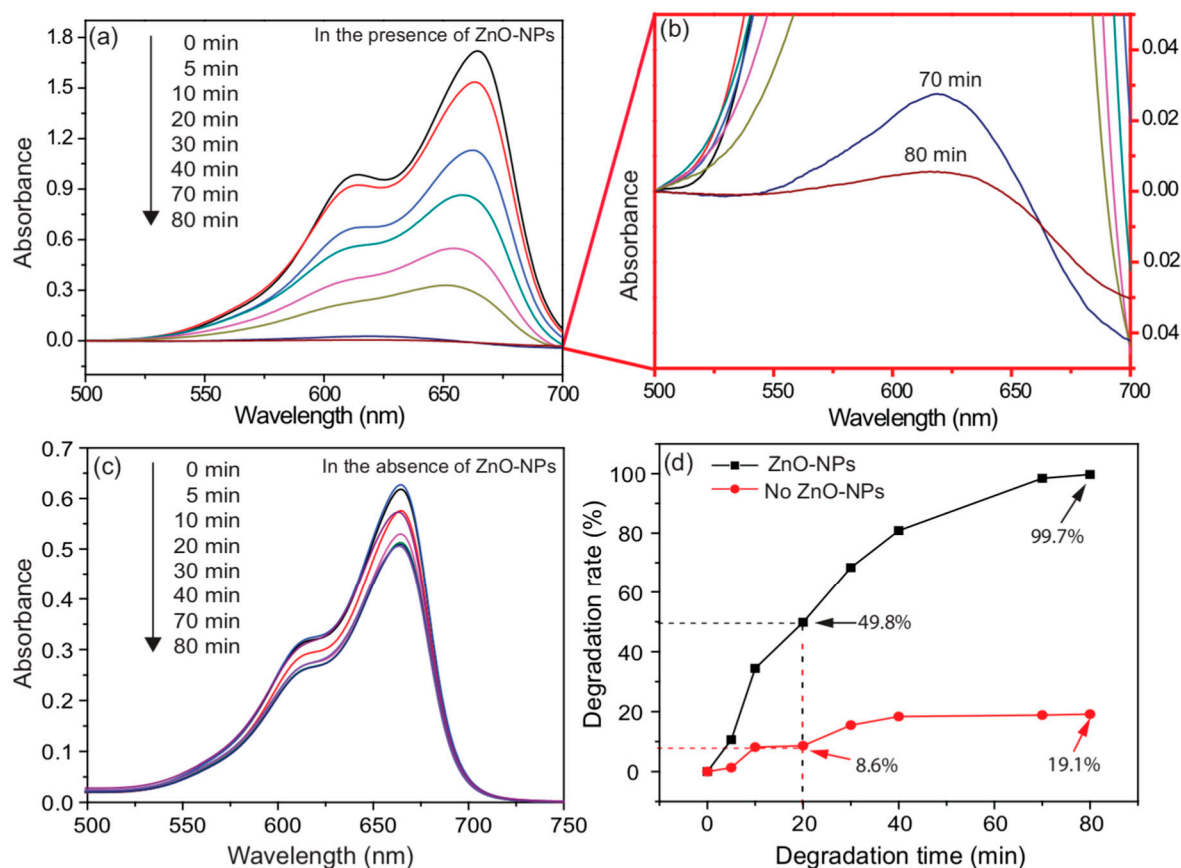


Figure 6. (a) UV-vis absorbance spectra showing the decomposition of methylene blue (MB) in the presence of ZnO-NPs, (b) a magnified view of the curves in panel (a), (c) UV-vis absorbance spectra of MB decomposition in the absence of ZnO-NPs, (d) degradation rates of MB in the presence or in the absence of ZnO-NPs. The decomposition of MB was carried out at 29 °C.

The kinetics of the photodegradation of MB was also investigated. The rate constants were obtained from the $\ln(C_0/C_t)$ vs time curves (Figure 7b). These curves show that the absorption peak intensity of the MB dye randomly decreased with increasing time, as already confirmed by the results in Figure 7a,b. Kinetic studies of the prepared ZnO-NPs were conducted, the results are presented in Figure 7b. The MB photodegradation reaction tends to exhibit pseudo-first-order kinetics described by Equation (2) [22]:

$$\ln(C_0/C_t) = kt \quad (2)$$

where C_0 is the absorbance at 0 min, C_t is the absorbance at decomposition time t , and k is the rate constant of the pseudo-first-order reaction. From Equation (2), we note that the direct relationship between the $\ln(C_0/C_t)$ and irradiation time (t) confirms the pseudo-first-order kinetics of the photodegradation of MB. The rate constant (k) was obtained from the slope of the equation of $\ln(C_0/C_t)$ vs. time, the calculated value was $0.0781 (\pm 0.01) \text{ min}^{-1}$. Other researchers have reported rate constant (k) values because they are correlated with photocatalytic activity. For example, Ren et al., who investigated the photocatalytic activity of ZnO and ZnO/Ag films in aqueous solution under UV irradiation for 90 min, reported calculated k values of 0.00516 min^{-1} and 0.00569 min^{-1} , respectively [26]. Li et al. described the photocatalytic activity of ZnO in aqueous solution under UV light and visible light for 150 min, their calculated k values were 0.0658 min^{-1} (UV light) and 0.00576 min^{-1} (visible light), respectively [27]. MB was used in both of the aforementioned studies. In the present work,

we investigated the photocatalytic activity of ZnO-NPs toward the degradation of MB in aqueous solution under UV light for 80 min, the k value was $0.0781 (\pm 0.01) \text{ min}^{-1}$. The higher the value of k , the greater the photocatalytic activity [28]. From this perspective, the k value of our experiment is higher than those described in the literature for the degradation of MB.

Table 1. Comparison of the photocatalytic activity of ZnO-NPs under different synthesis processes.

Catalyst	Preparation Method	Dye	Degradation Time (min)	Efficiency of Degradation (%)	Ref.
ZnO	Biological	Methyl red	180	92.5	[23]
ZnO	Biological	Methylene blue	90	83.45	[2]
ZnO	Biological	Methylene blue	180	97	[24]
Bare ZnO	Chemical	Methylene blue	120	37	[25]
Sr-doped ZnO	Chemical	Methylene blue	120	78.5	[10]
ZnO	Thermal	Methylene blue	80	99.71	this work

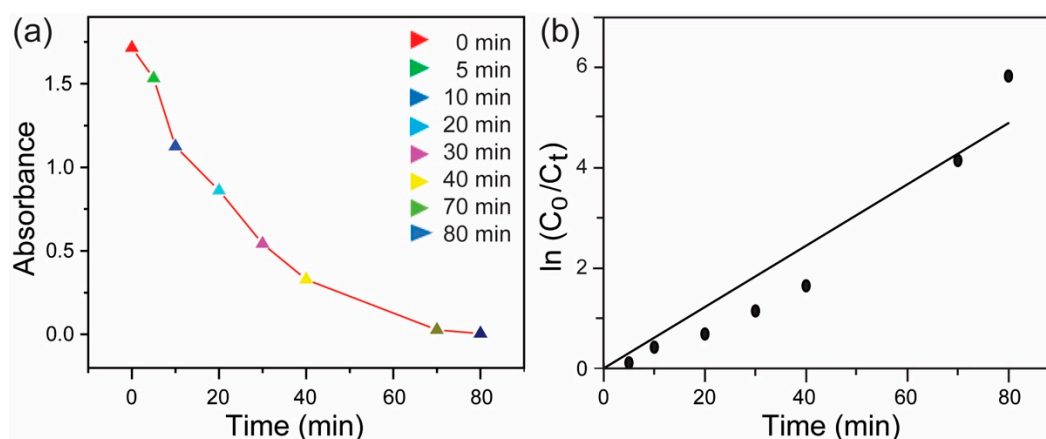


Figure 7. Photocatalytic performance of the ZnO-NPs: (a) absorbance vs time and (b) kinetic study for MB degradation (linear fitting data).

Several methods are available for increasing the rate of a photocatalytic reaction, including decreasing the bandgap, increasing the surface area, and increasing the defect concentration [1,29]. Hence, criteria such as the bandgap, surface area, crystallinity, particle size, and shape are important for achieving enhanced photocatalytic activity. A correlation exists between the bandgap and wavelength. Also, for the movement of electrons (photoexcited) from the VB to the CB, the wavelength is a notable factor. For the narrow bandgap of ZnO, longer-wavelength light is sufficient for photoexcitation. Our synthesized ZnO-NPs have a narrow bandgap (3.23 eV), as calculated from our UV-absorption spectra, consistent with the well-established agreement between a narrow bandgap and enhanced photocatalytic activity.

The catalyst surface is another important parameter affecting the photocatalytic reaction, because the reaction generally occurs on the catalyst's surface. If the catalytic surface area is increased, the likelihood of a reaction also increases. The smaller the particle size, the greater the surface area, which enhances the absorption of UV light and the photodecomposition of MB dye. Thus, photocatalytic activity is also enhanced through the synthesis of small-sized nanoparticles. According to the TEM observations, the synthesized ZnO-NPs were smaller than the pure ZnO particles. Also, from the XRD results, our ZnO-NPs exhibit high crystallinity, which further supports enhanced photocatalytic activity [22]. Our prepared ZnO-NPs showed excellent photocatalytic activity, which is attributable to the high purity of the ZnO. According to the XRD, EDS, and UV data, no impurities or elements were present in the prepared ZnO-NPs, which demonstrates that our product was highly pure.

Another important reason for enhanced photocatalytic activity is multiple light-scattering for spherical-shaped aggregated ZnO-NPs [30]. The light-scattering effect of nanoparticles strongly affects their photon-capture efficiency. For spherical-shaped aggregated ZnO-NPs, the light-scattering effect is increased. As a result, the photon-capture ability of such nanoparticles is also enhanced. In addition, a greater number of electrons from the VB quickly transfer to the CB, which can strongly influence the decomposition of organic pollutants and enhance the photocatalytic activity. The FE-SEM results (Figure 2) indicate that our prepared ZnO-NPs are aggregated spherical-shaped structures, this particle shape may be responsible for their enhanced photocatalytic activity.

A proposed photocatalytic mechanism for the catalytic degradation of MB dye by our synthesized ZnO-NPs is shown in Figure 8. The figure also displays the MB solution before (0 min) and after (80 min) the UV-light treatment. The blue color of the solution disappeared because of the reduction of MB. This result confirms that the ZnO-NPs displayed remarkable photocatalytic performance for the reduction of MB. When the UV light irradiates the ZnO-NPs' catalytic surface, electron-hole pairs are created on the catalytic surface, as represented in Equation (3):

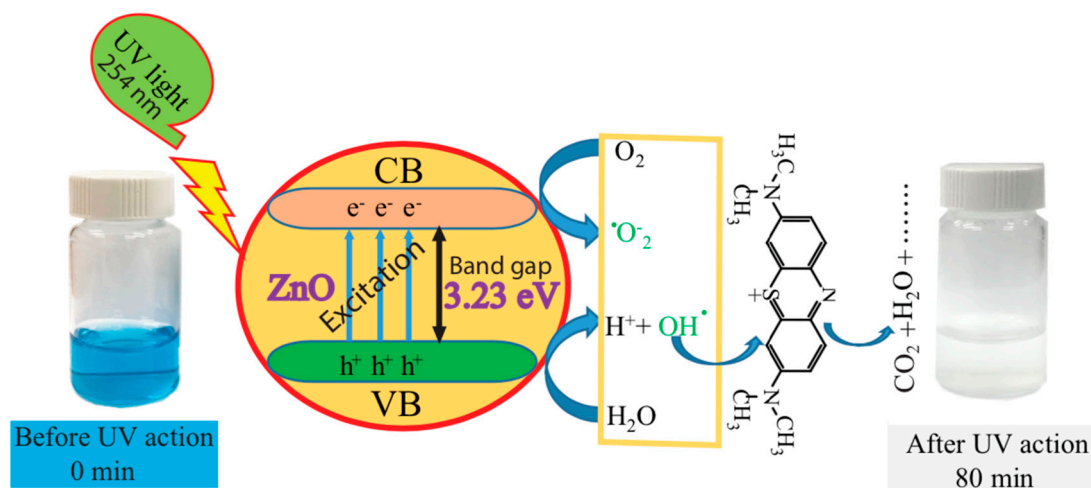
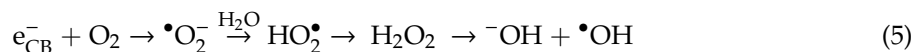


Figure 8. Proposed photocatalytic mechanism of ZnO-NPs for the catalytic degradation of MB dye.

In addition, VB electrons are transferred to the CB, thus generating an equal quantity of holes in the VB. In the VB, the active $\bullet\text{OH}$ free radicals are generated from H_2O molecules, as shown in Equation (4):



During the photoexcitation, $\bullet\text{O}_2^-$ free radicals are formed in the CB and these free radicals are eventually converted into $\bullet\text{OH}$ free radicals, as shown in Equation (5) [31]:



The decomposition of MB occurs via the active $\bullet\text{OH}$ free radicals:



The decomposition of MB may go through several steps up to produce CO_2 and H_2O finally. The decomposition of organic pollutants is followed by strong oxidants such as $\bullet\text{OH}$ radicals, which are represented in Figure 8 [32].

2.3. Antibacterial Performance of the Prepared ZnO-NPs

Bactericides promote rapid recovery from bacterial infection and also reduce the likelihood of bacteria developing drug resistance, which is why bactericidal agents are demanded in the medical field [33]. The tremendous inhibitory efficiency of ZnO-NPs against several pathogens has been documented elsewhere [34]. Figure 9 shows the antibacterial activity of ZnO-NPs against *E. coli*. In Figure 9, the broth liquid solution with 50 µg/mL, 200 µg/mL, 400 µg/mL, or 800 µg/mL of drug is clear in a visual inspection, indicating no growth of *E. coli*, whereas the solution with 0 µg/mL or 30 µg/mL is turbid, indicating the growth of *E. coli*. The minimum inhibitory concentration (MIC) of the ZnO-NPs solution toward *E. coli* was found to be 30–50 µg/mL. Thus, with increasing concentration, the antibacterial activity against *E. coli* was found to increase. ZnO-NPs are known to exhibit good antibacterial activity when present in high concentration as a consequence of their high surface area [35,36]. Our prepared ZnO-NPs show excellent antibacterial activity (MIC of 30–50 µg/mL) against *E. coli* compared with ZnO-NPs reported elsewhere (MICs of 500 µg/mL and 64 µg/mL). In previous works, the antibacterial activity of ZnO against *E. coli* was demonstrated with comparatively higher ZnO concentrations, which means that the ZnO in these previous papers was only effective at inhibiting bacterial growth at higher concentrations. Our product (ZnO-NPs), however, inhibits the growth of bacteria at comparatively lower concentrations. Therefore, we used our prepared ZnO-NPs as an antibacterial agent and then observed their performance at low concentrations. Table 2 summarizes the antibacterial activity of the ZnO-NPs against *E. coli*.

Table 2. The minimum inhibitory concentrations (MICs, µg/mL) of ZnO-NPs against *Escherichia coli* (*E. coli*).

Nanoparticles (NPs)	MIC (µg/mL) <i>Escherichia coli</i>	Ref.
ZnO-NPs	500	[34]
ZnO-NPs	64	[36]
ZnO-NPs	30~50	this work

Normally, the antibacterial mechanism of ZnO is discussed in view of specific processes. Also, the bactericidal mechanism of metal oxides is related to their photocatalytic properties. In the first process, when the reaction occurs between Zn and water, Zn is converted into Zn^{2+} , which participates in the decomposition of bacterial cells. The second process depends on the light catabolism, which mainly occurs under UV light, where ZnO induces the formation of active $\bullet OH$ free radicals. Bacteria have nucleic acids or respiratory enzymes that contain sulfhydryl groups, and these groups react with $\bullet OH$, resulting in inhibition of bacterial growth [37]. Also, the h^+ and e^- pairs of ZnO-NPs produce $\bullet OH$ and $\bullet O_2^-$ free radicals under irradiation with UV–vis light. The $\bullet OH$ free radical plays an important role in damaging the cell wall and cell membrane when it associates with the cell wall, $\bullet O_2^-$ reduces O_2 , causing substantial antibacterial activity [37].

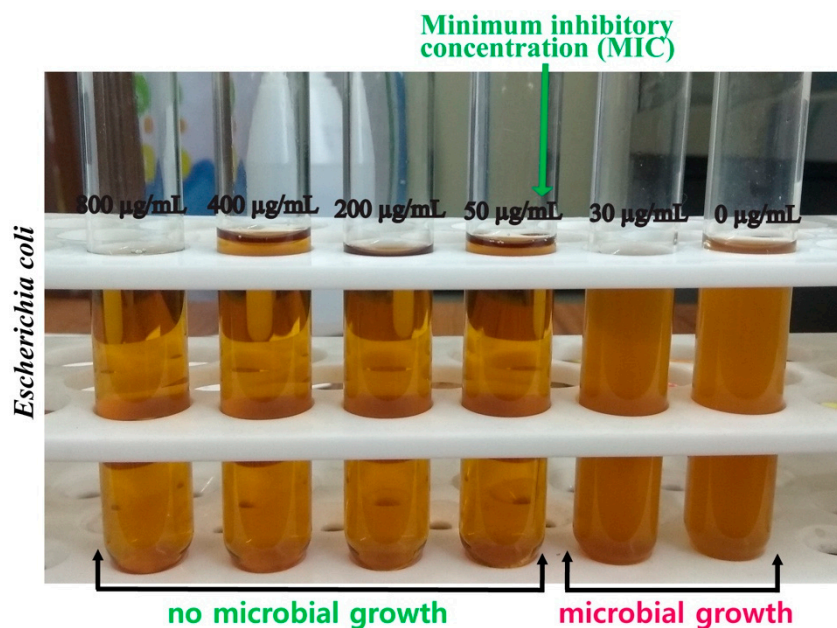


Figure 9. Antibacterial activity of the ZnO-NPs against *E. coli*.

Furthermore, antibacterial activity depends on the particle size, specific surface area, ion dissolution, crystallinity, and concentration, among other factors. Antibacterial activity increases with decreasing particle size [38]. However, in the case of a higher specific surface area, greater crystallinity, and higher concentration, the antibacterial activity is enhanced. These findings suggest that the small particle size, high specific surface area, and high crystallinity of ZnO-NPs should enhance their antibacterial activity. Hence, our synthesized ZnO-NPs exhibit excellent antibacterial activity.

Zinc oxide is harmful to the environment and is known to be toxic to aquatic organisms. On the other hand, small amounts suitable for the human body are used for therapeutic purposes as creams and ointments to prevent or treat sunburn and other skin irritations. The human safety of Zn-NPs synthesized in the current work is not clear yet, and further studies are needed. In the past, several studies on humans in the form of ZnO nanoparticles have been reported [39–44]. ZnO-NPs is harmful to microorganisms and may be highly biocompatible with human cells [39]. Very low oral toxicity, no irritation to eye or skin, and no risk of phototoxicity or photogenotoxicity to humans were also reported [40]. Akhtar et al. demonstrated in a cytotoxic assay that ZnO-NPs selectively induces cancer cell apoptosis among three types of human cancer cells and two types of primary rat cells [41]. Several reports have confirmed the absence of ZnO-NP cytotoxicity in different types of human/mammalian cells [42–44].

3. Experimental

3.1. Materials

ZAD [99.0%, Sigma-Aldrich, St. Louis, MO, USA] and pure zinc oxide (ZnO; 99.0%, Sigma-Aldrich, St. Louis, MO, USA) were used without further purification. The MB (high purity, biological stain, Heysham, Lancashire, UK) was acquired from Alfa Aesar.

3.2. Preparation of ZnO-NPs

ZnO-NPs were synthesized via a modified thermal method. One gram of ZAD was placed in a quartz crucible, which was subsequently placed in a stainless-steel chamber (made of SUS314) and sealed with an oxygen-free copper gasket (OFHC). The diameter and length of the chamber were 35 mm and 60 mm, respectively. Finally, the metal bolt-sealed chamber was placed in a furnace (KSL-1100X-S-UL-LD, Richmond, CA, USA) in which the temperature was maintained at 550 °C for

10 h. After thermolysis, the furnace was slowly cooled to room temperature over a period of 4 h to induce the smooth and uniform production of ZnO-NPs. Figure S5 shows the whole procedure for the preparation of the ZnO-NPs. Various analyses showed that our synthesized product contained ZnO, with no other elements or phases. The likely reaction mechanism leading to the ZnO-NPs is presented as follows:



3.3. Characterization of the Structure and Composition of the Prepared ZnO-NPs

The prepared ZnO-NPs were characterized by several techniques. The crystal structure, purity, and phase composition of the ZnO-NPs were analyzed by multipurpose high-performance XRD (PANalytical, X'Pert PRO, Netherlands). The XRD pattern was recorded using Cu K α radiation with a wavelength of 1.5406 Å, the scan range was $20 \leq 2\theta \leq 90^\circ$. The whole morphological shape and the size of the prepared ZnO-NPs were characterized by TEM (JEOL, JEM-2010, Japan). The ZnO-NP powder was dispersed in distilled water and sonicated in an ultrasonic bath (Power Sonic 450, Republic of Korea) for 30 min. The suspension of ZnO-NPs was then dropped onto a standard carbon-coated copper grid (200 mesh) and dried in the air for 4 h for TEM observation. FE-SEM (Carl Zeiss, SUPRA 40VP, Oberkochen, Germany) was also used to characterize the morphology of the NPs. To check their chemical composition (purity), their energy-dispersive X-ray spectrum was recorded. The light-absorption properties of the prepared ZnO-NPs were characterized by UV-vis spectroscopy (Perkin Elmer Lambda 25, Ayer Rajah, Singapore). The thermogravimetric analysis (TG/DTA) was carried out on a thermal analysis instrument (TA Instruments SDT Q600 V20.9 Build 20, New Castle, DE, USA).

3.4. Photocatalytic Performance

An MB solution (1.5 mg of MB in 200 mL of distilled water) was used. Ten milligrams of the ZnO-NP powder were added to the MB solution, and the suspension was stirred using a magnetic stirrer for 90 min. It was then stored in a dark room for 60 min to reach equilibrium. The photocatalytic performance of the prepared ZnO-NP powder was monitored through the photodegradation of an MB solution in the presence of UV radiation. The reaction was carried out under an 80 mW/cm² UV lamp (FNS TECH, Republic of Korea) with an emission wavelength of 254 nm. To monitor the decomposition of the MB, fixed-volume MB samples were collected at different time intervals and their UV-vis absorption spectrum was recorded. The same procedure was used to characterize the photocatalytic performance of pure ZnO.

3.5. Antibacterial Screening

The antibacterial screening of the prepared ZnO-NPs was carried out against *E. coli* pathogenic microbial strain by accessing growth inhibition. We used a microbroth dilution method [36] to determine the MIC of the prepared ZnO-NPs. Specifically, the ZnO-NPs were added at six different concentrations for *E. coli* (800 µg/mL, 400 µg/mL, 200 µg/mL, 50 µg/mL, 30 µg/mL, 0 µg) in separate sterile 50 mL Falcon tubes containing 10 mL of sterile nutrient broth. One hundred microliters of fresh culture of *E. coli* (adjusted with McFarland standard) was added in a 10 mL nutrient broth in each of the six Falcon tubes under sterile conditions. The tubes were then subjected to shaking at 150 rpm using a shaker incubator for 20 h. The broth liquids were collected in six separate sterile test tubes for observation.

4. Conclusions

A ZnO-NP photocatalyst and antimicrobial agent was synthesized via an environmentally safe and cost-effective thermal method. FE-SEM and TEM analyses revealed that the synthesized particles are smooth and spherical, with a nearly aggregated size distribution. The XRD patterns indicated that the ZnO-NPs crystallized in the hexagonal wurtzite structure with high crystallinity. The UV absorption spectra showed a marked redshift. Photocatalytic activity tests revealed that our product exhibits an excellent degradation percentage (99.7%) within a short time (80 min). Within 20 min, 50% of MB dye was degraded. Also, the antibacterial activity investigation revealed that the MIC of the ZnO-NPs against *E. coli* was 30–50 µg/mL. Therefore, our reported product prevents the growth of *E. coli* at a low concentration, demonstrating better antibacterial performance than previously reported ZnO-NPs. The results presented here suggest that our unique synthesis method warrants further investigation.

Supplementary Materials: The following are available online at <http://www.mdpi.com/2073-4344/9/7/608/s1>, Figure S1. (a) and (b) FE-SEM images of the pure ZnO (ACS reagent) at different magnifications, Figure S2. (a) and (b) TEM images of the pure ZnO (ACS reagent) at different magnifications, Figure S3. UV-vis absorption spectrum of synthesized ZnO-NPs in the range 200–900 nm, Figure S4. UV-vis absorbance spectra showing the decomposition of methylene blue (MB) in the presence of (a) the ZnO-NPs and (b) the pure ZnO (ACS reagent); (c) degradation rates of MB and (d) kinetic plots in presence of the ZnO-NPs or the pure ZnO. The rate constant (k) was obtained from the slope of the equation of absorbance vs. time; the calculated value was $0.0781 (\pm 0.01) \text{ min}^{-1}$ in the presence of the ZnO-NPs and $0.0224 (\pm 0.01) \text{ min}^{-1}$ in the presence of the pure ZnO, respectively. The decomposition of MB was carried out at 29 °C, Figure S5. Schematic diagram for preparation of ZnO-NPs.

Author Contributions: Conceptualization, M.A.H. and J.R.H.; experiment design, M.A.H. and J.R.H.; data analysis, M.A.H., I.L., J.A. and A.A.S.M.Z., writing-original draft preparation, M.A.H. and J.R.H.; writing-review and editing, M.A.H., J.A., M.A.I., K.P.S. and J.R.H.; supervision, J.R.H.

Funding: This work was supported by the Korean Government, NRF-2018R1A2B6006155.

Conflicts of Interest: The authors declare no conflict of interest.

References

1. Etacheri, V.; Roshan, R.; Kumar, V. Mg-doped ZnO nanoparticles for efficient sunlight-driven photocatalysis. *ACS Appl. Mater. Interfaces* **2012**, *4*, 2717–2725. [[CrossRef](#)] [[PubMed](#)]
2. Zheng, Y.; Fu, L.; Han, F.; Wang, A.; Cai, W.; Yu, J.; Yang, J.; Peng, F. Green biosynthesis and characterization of zinc oxide nanoparticles using *Corymbia citriodora* leaf extract and their photocatalytic activity. *Green Chem. Chem. Lett. Rev.* **2015**, *8*, 59–63. [[CrossRef](#)]
3. Vlad, S.; Tanase, C.; Macocinschi, D.; Ciobanu, C.; Balaes, T.; Filip, D.; Gostin, I.N.; Gradinaru, L.M. Antifungal behaviour of polyurethane membranes with zinc oxide nanoparticles. *Dig. J. Nanomater. Biostruct.* **2012**, *7*, 51–58.
4. Akbar, A.; Sadiq, M.B.; Ali, I.; Muhammad, N.; Rehman, Z.; Khan, M.N.; Muhammad, J.; Khan, S.A.; Rehman, F.U.; Anal, A.K. Synthesis and antimicrobial activity of zinc oxide nanoparticles against foodborne pathogens *Salmonella typhimurium* and *Staphylococcus aureus*. *Biocat. Agri. Biotech.* **2019**, *17*, 36–42. [[CrossRef](#)]
5. Jiang, W.T.; Wu, C.T.; Sung, Y.H.; Wu, J.J. Room-temperature fast construction of outperformed ZnO nanoarchitectures on nanowire-array templates for dye-sensitized solar cells. *ACS Appl. Mater. Interfaces* **2013**, *5*, 911–917. [[CrossRef](#)] [[PubMed](#)]
6. Seager, C.H.; Warren, W.L.; Tallant, D.R.; Voigt, J.A. Correlation between photoluminescence and oxygen vacancies in ZnO phosphors. *Appl. Phys. Lett.* **1996**, *68*, 403–405.
7. Wu, J.J.; Liu, S.C. Low-temperature growth of well-aligned ZnO nanorods by chemical vapor deposition. *Adv. Mater.* **2002**, *14*, 215–218. [[CrossRef](#)]
8. Guo, L.; Ji, Y.L.; Xu, H. Regularly shaped, single-crystalline ZnO nanorods with wurtzite structure. *J. Am. Chem. Soc.* **2002**, *124*, 14864–14865. [[CrossRef](#)]
9. Mari, B.; Mollar, M.; Mechkour, A.; Hartiti, B.; Perales, M.; Cembrero, L. Optical properties of nanocolumnar ZnO crystals. *Microelectron. J.* **2004**, *35*, 79–82. [[CrossRef](#)]

10. Yousefi, R.; Farid, J.-S.; Cheraghizade, M.; Sara, K.-G.; Saaedi, A.; Huang, N.M.; Basirun, W.J.; Azarang, M. Enhanced visible-light photocatalytic activity of strontium-doped zinc oxide nanoparticles. *Mater. Sci. Semi. Proc.* **2015**, *32*, 152–159. [[CrossRef](#)]
11. Kislov, N.; Lahiri, J.; Verma, H.; Goswami, D.Y.; Stefanakos, E.; Batzill, M. Photocatalytic degradation of methyl orange over single crystalline ZnO: Orientation dependence of photoactivity and photostability of ZnO. *Langmuir* **2009**, *25*, 3310–3315. [[CrossRef](#)] [[PubMed](#)]
12. Bu, Y.; Chen, Z.; Li, W.; Hou, B. Highly efficient photocatalytic performance of graphene–ZnO quasi-shell-core composite material. *ACS Appl. Mater. Interfaces* **2013**, *5*, 12361–12368. [[CrossRef](#)] [[PubMed](#)]
13. Hossain, M.M.; Ku, B.-C.; Hahn, J.R. Synthesis of an efficient white-light photocatalyst composite of graphene and ZnO nanoparticles: Application to methylene blue dye decomposition. *App. Surf. Sci.* **2015**, *354*, 55–65. [[CrossRef](#)]
14. Sharma, D.; Rajput, J.; Kaith, B.S.; Kaur, M.; Sharma, S. Synthesis of ZnO nanoparticles and study of their antibacterial and antifungal properties. *Thin Solid Films* **2010**, *5*, 191224–191229. [[CrossRef](#)]
15. JCPDS. Powder Diffraction File, Alphabetical Index, Inorganic Compounds, International Centre for Diffraction Data. Newtown Square, PA, USA, 1977. Available online: <http://www.icdd.com> (accessed on 15 July 2019).
16. Moharram, A.H.; Mansour, S.A.; Hussein, M.A.; Rashad, M. Direct precipitation and characterization of ZnO nanoparticles. *J. Nanomat.* **2014**, *2014*, 1–5. [[CrossRef](#)]
17. Umara, A.; Rahman, M.M.; Al-Hajry, A.; Hahn, Y.-B. Highly-sensitive cholesterol biosensor based on well-crystallized flower-shaped ZnO nanostructures. *Talanta* **2009**, *78*, 284–289. [[CrossRef](#)]
18. Vaseem, M.; Lee, K.-M.; Shin, J.-K.; Hahn, Y.B. Synthesis of ZnO nanoparticles and their ink-jetting behavior. *J. Nanosci. Nanotechnol.* **2012**, *12*, 2380–2386. [[CrossRef](#)]
19. Hossain, M.M.; Hossain, S.; Seungbae, S.; Hahn, J.R. In situ fabrication of a thermally stable and highly porous conductive solar light-driven ZnO-CNT fiber photocatalyst. *RSC Adv.* **2016**, *6*, 71450–71460. [[CrossRef](#)]
20. Zak, A.K.; Youefi, R.; Majid, W.H.A.; Muhamad, M.R. Facile synthesis and X-ray peak broadening studies of Zn_{1-x}Mg_xO nanoparticles. *Ceram. Int.* **2012**, *38*, 2056–2064.
21. Arii, T.; Kishi, A. The effect of humidity on thermal process of zinc acetate. *Thermochim. Acta* **2003**, *400*, 175–185. [[CrossRef](#)]
22. Yang, C.; Li, Q.; Tang, L.; Xin, K.; Bai, A.; Yu, Y. Synthesis, photocatalytic activity, and photogenerated hydroxyl radicals of monodisperse colloidal ZnO nanospheres. *Appl. Surf. Sci.* **2015**, *357*, 1928–1938. [[CrossRef](#)]
23. Fu, L.; Fu, Z. *Plectranthus amboinicus* leaf extract-assisted biosynthesis of ZnO nanoparticles and their photocatalytic activity. *Ceram. Int.* **2015**, *41*, 2492–2496. [[CrossRef](#)]
24. Nava, O.J.; Soto-Robles, C.A.; Gomez-Gutierrez, C.M.; Vilchis-Nestor, A.R.; Castro-Beltran, A.; Olivas, A.; Luque, P.A. Fruit peel extract mediated green synthesis of zinc oxide nanoparticles. *J. Molec. Struct.* **2017**, *1147*, 1–6. [[CrossRef](#)]
25. Azarang, M.; Shuhaimi, A.; Yousefi, R.; Jahromi, S.P. One-pot sol–gel synthesis of reduced graphene oxide uniformly decorated zinc oxide nanoparticles in starch environment for highly efficient photodegradation of methylene blue. *RSC Adv.* **2015**, *5*, 21888–21896. [[CrossRef](#)]
26. Ren, C.; Yang, B.; Wu, M.; Xu, J.; Fu, Z.; Lv, Y.; Guo, T.; Zhao, Y.; Zhu, C. Synthesis of Ag/ZnO nanorods array with enhanced photocatalytic performance. *J. Hazard. Mater.* **2010**, *182*, 123–129. [[CrossRef](#)]
27. Li, J.; Yan, J.; Liu, C.; Dong, L.; Lv, H.; Sun, W.; Xing, S. Manipulation on ZnO heterostructures: from binary ZnO–Ag to ternary ZnO–Ag–polypyrrole. *Cryst. Eng. Comm.* **2014**, *16*, 10943–10948. [[CrossRef](#)]
28. Wang, L.; Chang, L.; Zhao, B.; Yuan, Z.; Shao, G.; Zheng, W. Systematic investigation on morphologies, forming mechanism, photocatalytic and photoluminescent properties of zno nanostructures constructed in ionic liquids. *Inorg. Chem.* **2008**, *47*, 1443–1452. [[CrossRef](#)] [[PubMed](#)]
29. Li, D.; Huang, J.-F.; Cao, L.Y.; LI, J.-Y.; OuYang, H.-B.; Yao, C.-Y. Microwave hydrothermal synthesis of Sr²⁺ doped ZnO crystallites with enhanced photocatalytic properties. *Ceram. Int.* **2014**, *40*, 2647–2653. [[CrossRef](#)]
30. Zhang, Q.; Chou, T.P.; Russo, B.; Jenekhe, S.A.; Cao, G. Polydisperse aggregates of ZnO nanocrystallites: A method for energy-conversion-efficiency enhancement in dye-sensitized solar cells. *Adv. Funct. Mater.* **2008**, *18*, 1654–1660. [[CrossRef](#)]
31. Houas, A.; Lachheb, H.; Ksibi, M.; Elaloui, E.; Guillard, C.; Herrmann, J.-M. Photocatalytic degradation pathway of methylene blue in water. *Appl. Catal. B* **2001**, *31*, 145–157. [[CrossRef](#)]

32. Zong, Y.; Li, Z.; Wang, X.; Ma, J.; Men, Y. Synthesis and high photocatalytic activity of Eu-doped ZnO nanoparticles. *Ceram. Int.* **2014**, *40*, 10375–10382. [[CrossRef](#)]
33. French, G.L. Bactericidal agents in the treatment of MRSA infections—the potential role of daptomycin. *J. Antimicrob. Chemother.* **2006**, *58*, 1107–1117. [[CrossRef](#)] [[PubMed](#)]
34. Ansari, M.A.; Khan, H.M.; Khan, A.A.; Sultan, A.; Azam, A. Synthesis and characterization of the antibacterial potential of ZnO nanoparticles against extended-spectrum β -lactamases-producing *Escherichia coli* and *Klebsiella pneumoniae* isolated from a tertiary care hospital of North India. *Appl. Microbiol. Biotechnol.* **2012**, *94*, 467–477. [[CrossRef](#)] [[PubMed](#)]
35. Zhang, L.; Jiang, Y.; Ding, Y.; Povey, M.; York, D. Investigation into the antibacterial behaviour of suspensions of ZnO nanoparticles (ZnO nanofluids). *J. Nanopart. Res.* **2007**, *9*, 479–489. [[CrossRef](#)]
36. Shankar, S.; Rhim, J.-W. Facile approach for large-scale production of metal and metal oxide nanoparticles and preparation of antibacterial cotton pads. *Carbohydr. Polym.* **2017**, *163*, 137–145. [[CrossRef](#)] [[PubMed](#)]
37. Zhou, G.; Li, Y.; Xiao, W.; Zhang, L.; Zuo, Y.; Xue, J.; Jansen, J.A. Synthesis, characterization, and antibacterial activities of a novel nanohydroxyapatite/zinc oxide complex. *J. Biomed. Mater. Res. Part A* **2008**, *85*, 929–937. [[CrossRef](#)]
38. Raghupathi, K.R.; Koodali, R.T.; Manna, A.C. Size-dependent bacterial growth inhibition and mechanism of antibacterial activity of zinc oxide nanoparticles. *Langmuir* **2011**, *27*, 4020–4028. [[CrossRef](#)]
39. Padmavathy, N.; Vijayaraghavan, R. Enhanced bioactivity of ZnO nanoparticles—An antimicrobial study. *Sci. Technol. Adv. Mater.* **2008**, *9*, 035004. [[CrossRef](#)]
40. Schilling, K.; Bradford, B.; Castelli, D.; Dufour, E.; Nash, J.F.; Pape, W.; Schulte, S.; Ian Tooley, I.; Bosch, J.V.D.; Schellauf, F. Human safety review of “nano” titanium dioxide and zinc oxide. *Photochem. Photobiol. Sci.* **2010**, *9*, 495–509. [[CrossRef](#)]
41. Akhtar, M.J.; Ahamed, M.; Kumar, S.; Khan, M.M.; Ahmad, J.; Alrokayan, S.A. Zinc oxide nanoparticles selectively induce apoptosis in human cancer cells through reactive oxygen species. *Int. J. Nanomed.* **2012**, *7*, 845–857.
42. Wu, W.; Samet, J.M.; Peden, D.B.; Bromberg, P.A. Phosphorylation of p65 is required for zinc oxide nanoparticle-induced interleukin 8 expression in human bronchial epithelial cells. *Environ. Health Perspect.* **2010**, *118*, 982–987. [[CrossRef](#)]
43. Kocbek, P.; Teskac, K.; Kreft, M.E.; Kristl, J. Toxicological aspects of long-term treatment of keratinocytes with ZnO and TiO₂ nanoparticles. *Small* **2010**, *6*, 1908–1917. [[CrossRef](#)]
44. Meyer, K.; Rajanahalli, P.; Ahamed, M.; Rowe, J.J.; Hong, Y. ZnO nanoparticles induce apoptosis in human dermal fibroblasts via p53 and p38 pathways. *Toxicol. In Vitro* **2011**, *25*, 1721–1726. [[CrossRef](#)]

